



***In situ* study of the precursor conversion reactions during solventless thermolysis of Co<sub>9</sub>S<sub>8</sub>, Ni<sub>3</sub>S<sub>2</sub>, Co and Ni nanowires**

Journal:	<i>Nanoscale</i>
Manuscript ID	NR-ART-03-2018-002093.R1
Article Type:	Paper
Date Submitted by the Author:	30-Jul-2018
Complete List of Authors:	Scott, John; University of Technology Sydney, Maths and Physical Sciences Angeloski, Alexander; UTS, Australia, School of Mathematical and Physical Sciences Aharonovich, Igor; University of Technology, Sydney, Lobo, Charlene; University of Technology Sydney, Maths and Physical Sciences McDonagh, Andrew; UTS, Australia, School of Mathematical and Physical Sciences Toth, Milos; University of Technology, Sydney, School of Physics and Advanced Materials



## Journal Name

## ARTICLE

## *In situ* study of the precursor conversion reactions during solventless thermolysis of Co<sub>9</sub>S<sub>8</sub>, Ni<sub>3</sub>S<sub>2</sub>, Co and Ni nanowires

John A. Scott,<sup>a\*</sup> Alexander Angeloski,<sup>a</sup> Igor Aharonovich,<sup>a</sup> Charlene J. Lobo,<sup>a</sup> Andrew McDonagh<sup>a\*</sup> and Milos Toth<sup>a\*</sup>

Received 00th January 20xx,  
Accepted 00th January 20xx

DOI: 10.1039/x0xx00000x

www.rsc.org/

Synthesis of Co<sub>9</sub>S<sub>8</sub>, Ni<sub>3</sub>S<sub>2</sub>, Co and Ni nanowires by solventless thermolysis of a mixture of metal(II) acetate and cysteine in vacuum is reported. The simple precursor system enables the nanowire phase to be tuned from pure metal (Co or Ni) to metal sulfide (Co<sub>9</sub>S<sub>8</sub>, Ni<sub>3</sub>S<sub>2</sub>) by varying the relative concentration of the metal(II) acetate. The growth environment facilitates new insights through *in situ* characterization using field-emission scanning electron microscopy (FESEM) and thermogravimetric analysis with gas chromatography-mass spectrometry (TGA-GC-MS). Direct observation by FESEM shows the temperature at which nanowire growth occurs and suggests adatoms are incorporated into the base of the growing nanowire. TGA-GC-MS reveals the rates of precursor decomposition and identity of the volatilized ligand fragments during heat-up and at the nanowire growth temperature. Our results constitute a new approach for the selective fabrication of high quality Co<sub>9</sub>S<sub>8</sub> and Ni<sub>3</sub>S<sub>2</sub> nanowires and more importantly provides new understanding of precursor decomposition reactions that support symmetry-breaking growth in nanocrystals by heat-up synthesis.

### Introduction

Colloidal synthesis by hot-injection and heat-up coprecipitation techniques are powerful methods for achieving monodisperse nanocrystals with controllable size, morphology and composition.<sup>1-6</sup> An understanding of the precursor conversion reactions is crucial to expanding the scope of these techniques to new material systems and morphologies.<sup>6-10</sup> To date, few reports have examined the reactivity of precursors that support anisotropic growth highlighting the need for *in situ* characterization.<sup>9, 11, 12</sup> Characterization of the reactions during nanocrystal growth is challenging due to the speed at which transformations occur, and solvent effects.<sup>13-15</sup> *In situ* characterization studies have utilized mostly UV-vis absorbance and nuclear magnetic resonance spectroscopies in the solution state, although these techniques can suffer due to lack of sensitivity (in NMR), the generation of optically transparent species, anomalous extinction due to scattering, and temperature dependent optical properties of nanocrystals.<sup>16-23</sup>

Solventless thermolysis is a versatile sub-set of coprecipitation techniques that enables crystal growth under straightforward conditions, and has been used to synthesize high quality copper, nickel, lead and bismuth sulfide nanocrystals of

various morphologies with narrow size distributions.<sup>24-28</sup> Only a few direct bottom-up syntheses have been reported for Co<sub>9</sub>S<sub>8</sub> nanocrystals including nanowires.<sup>29, 30</sup> Rather, most reported techniques utilize a multi-step method whereby a metal oxide structure is first formed and the sulfide phase is produced by exchange of the oxygen atoms for sulfur.<sup>29, 31-33</sup> The morphology is heavily influenced by the intermediate cobalt oxide nanocrystal, and often hollowing of the nanostructure by the Kirkendall effect is observed.<sup>33-35</sup>

Real-time characterization has led to significant breakthroughs in fundamental understanding of nanocrystal growth. Utilizing the reaction environment for solventless thermolysis enables studying the reaction steps by electron microscopy and TGA-GC-MS. Advances through electron microscopy studies include observation of multistep nucleation pathways, measured nanowire growth kinetics, observation of layer-by-layer growth in nanowires and morphological changes owing to catalyst migration (VLS growth).<sup>36-40</sup> However slow progress has been made as typical reaction conditions are inherently incompatible with high resolution imaging conditions (i.e. wet environments, elevated pressures, and high temperatures). Nanocrystal growth by solventless thermolysis overcomes many of the challenges presented from solution or vapor phase precursors.

<sup>a</sup> School of Mathematical and Physical Sciences, University of Technology Sydney, Ultimo 2007, Australia

† Footnotes relating to the title and/or authors should appear here.

Electronic Supplementary Information (ESI) available: [details of any supplementary information available should be included here]. See DOI: 10.1039/x0xx00000x



**Figure 1** Schematic illustrating nanowire synthesis:  $M^{II}$  acetate ( $M = \text{Co}, \text{Ni}$ ) and  $M^{II}$  bis-cysteinate ( $M^{II}Cys_2$ ) in aqueous solution are dropcast onto a silicon wafer. Nanowire growth of the  $M^0$  and/or  $M_xS_y$  phase is achieved by annealing in high vacuum with the nanowire phase determined by the  $M^{II}:\text{Cys}$  mole ratio.

In our previous work, we showed that various thiol sources act as efficient capping ligands to support nanowire growth.<sup>41</sup> The unique properties of nanowires make them important as active materials in catalysis,<sup>42</sup> photodetectors,<sup>43,44</sup> high density magnetic data storage<sup>45</sup> and beyond.<sup>46, 47</sup> In this paper an examination of the growth precursors used in a high-vacuum thermolysis technique that yields nanowires of  $\text{Co}_9\text{S}_8$ ,  $\text{Ni}_3\text{S}_2$ , Co and Ni is provided. Metal(II/III) bis-cysteinate and metal(II) acetate (where metal = cobalt or nickel) were used to examine the influence of their relative concentrations on the resultant nanowire phase. *In situ* characterization of the thermolysis behaviour of the precursors was examined using FESEM and TGA-GC-MS. The results reveal (in both precursor systems) a single-step mass loss event to yield  $M_xS_y$  species followed by a slow loss of sulfur species at nanowire growth temperature. Sulfur species are known capping ligands that can support anisotropic crystal growth and provide control over the resultant crystal morphology.<sup>27, 48, 49</sup> Capping ligands are typically either added to growth precursors, or generated *in situ* as reaction by-products during nanocrystal growth. The latter approach, employed here, is advantageous due to the ability to eliminate side reactions, greater precursor air stability (relative to metal alkyls), and ease of manipulation.<sup>50-52</sup> Our results constitute a new approach for the selective fabrication of high quality  $\text{Co}_9\text{S}_8$  and  $\text{Ni}_3\text{S}_2$  nanowires, which have compelling applications in optoelectronics,<sup>53</sup> advanced energy storage and conversion<sup>54, 55</sup> and catalysis.<sup>56, 57</sup> Moreover, our findings provide insights into the precursor conversion rates and byproducts that support anisotropic crystal growth by solventless thermolysis.

## Results

**Synthesis of Nanowires.** Commercially available cobalt(II) acetate tetrahydrate, nickel(II) acetate tetrahydrate and L-cysteine (Cys) were employed as metal and sulfur sources for the growth of Co and Ni nanowires, and their sulfide phases pentlandite ( $\text{Co}_9\text{S}_8$ ) and heazlewoodite ( $\text{Ni}_3\text{S}_2$ ). In a typical growth procedure, a solution containing the precursor compounds is dropcast onto a clean silicon substrate with a native oxide layer (Figure 1). After air-drying, the specimen is

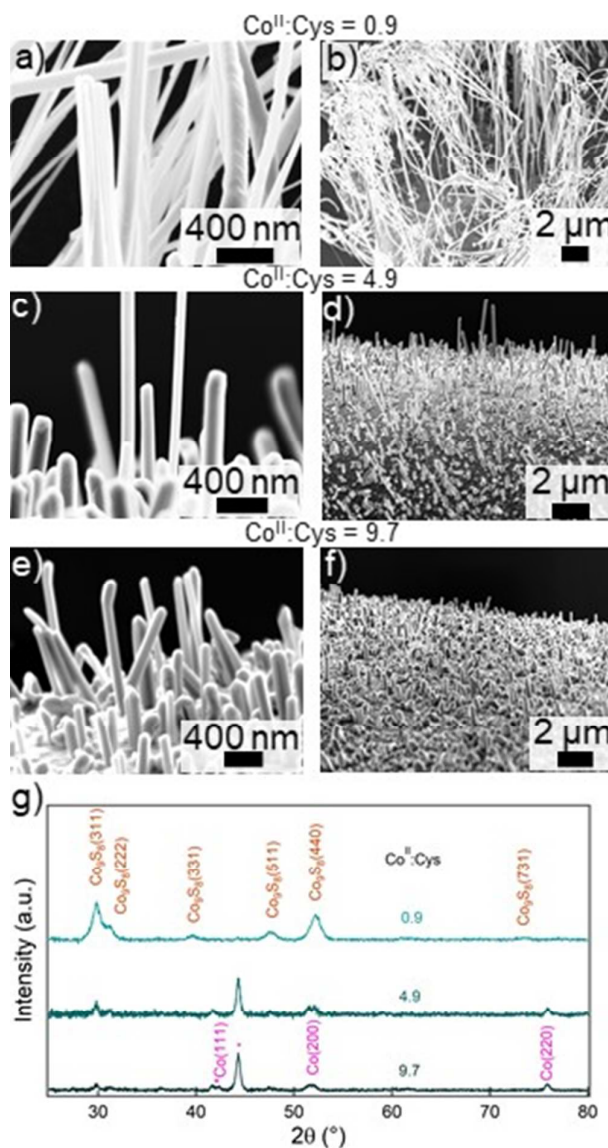


**Figure 2** SEM images of  $\text{Co}_9\text{S}_8$  and Co nanostructures grown from  $\text{Co}^{II}:\text{Cys}$  solutions with mole ratios of 0.9 (a and b), 4.9 (c and d) and 9.7 (e and f). g) X-ray diffraction patterns of growth products from the three solutions.

loaded into a high-vacuum annealing chamber and evacuated to a pressure of  $10^{-7}$  mbar (precipitation of nanocrystals was not observed). The sample is heated to a growth temperature at a rate of  $2 - 3$  °C/sec, and annealed before cooling to room temperature. The annealing temperature for  $\text{Co}_9\text{S}_8/\text{Co}$  nanowire growth was  $590 \pm 20$  °C, and the total annealing time at this temperature was 1 hour (a typical plot of the temperature measured as a function of time during heat-up and growth is shown in Figure S1). Precursor compounds for  $\text{Ni}_3\text{S}_2/\text{Ni}$  nanowire growth were annealed for 5 hours at  $415 \pm 10$  °C (a description of the synthesis method can be found in the Supporting Information). The cysteine concentration in the precursor solution was kept constant at  $9.0 \pm 0.5$  mM and the amount of metal(II) acetate was varied to achieve  $M^{II}:\text{Cys}$  mole ratios in the range 0.9 - 9.7.

We show that the nanowire phase can be tuned between pure metal ( $\text{Co}^0$  or  $\text{Ni}^0$ ) and metal sulfide by adjusting the relative concentration of the metal(II/III) bis-cysteinate complex and metal(II) acetate, which is achieved by varying the mole ratios of the  $\text{M}^{\text{II}}$  (metal(II) acetate) and S (cysteine) reagents.

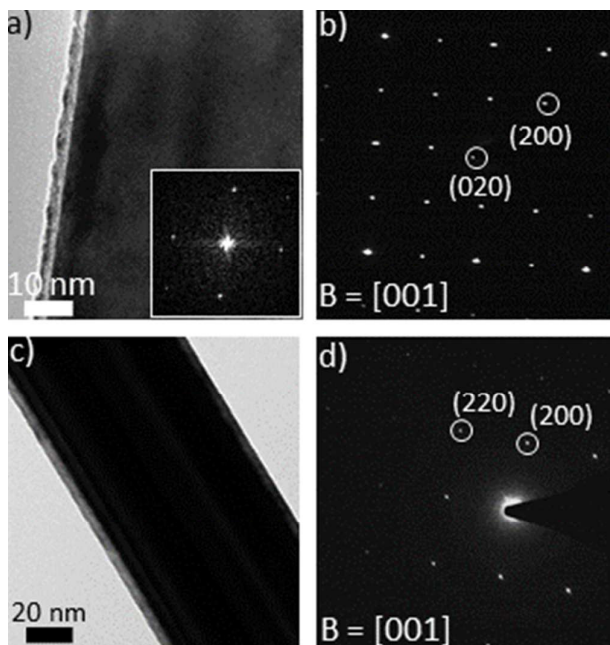


**Figure 3a)** TEM image of a  $\text{Co}_9\text{S}_8$  nanowire with FFT (inset). **b)** SAED pattern of nanowire in a). **c)** TEM image of a Co nanowire. **d)** SAED pattern of nanowire in c).

**Nanowire Morphology, Structure and Composition.** Data obtained using nanowires from thermolysis of 0.9, 4.9 and 9.7  $\text{Co}^{\text{II}}:\text{Cys}$  mole ratio solutions are shown in Figure 2. Figures 2a and b show typical morphology of nanowires grown from a 0.9 ( $\text{Co}^{\text{II}}:\text{Cys}$ ) precursor solution, with the X-ray diffraction pattern (Figure 2g) matching face-centred cubic (FCC)  $\text{Co}_9\text{S}_8$  (PDF 04-004-4525). Minor peak intensities were indexed to FCC  $\text{Co}^0$  (PDF 00-015-0806). The nanowires have a broad diameter distribution with a mean of 125 nm based on an analysis of 82 structures (Figure S2). The variation in length was considerable with a number of nanowires extending over 20  $\mu\text{m}$  with an aspect ratio > 400, the average was 5.4  $\mu\text{m}$  (Figure S3). Nanowire morphologies from 4.9 and 9.7 ( $\text{Co}^{\text{II}}:\text{Cys}$ ) solutions are shown in Figures 2c-d, and Figures 2e-f respectively. Characterization by X-ray diffraction shows the dominant phase to be FCC Co (PDF 00-015-0806) with a minor presence of FCC  $\text{Co}_9\text{S}_8$  (Figure 2g). The 4.9 ( $\text{Co}^{\text{II}}:\text{Cys}$ ) solution produced nanowires and nanorods with a mean diameter of 130 nm based on an analysis of 47 structures (Figure S4), with an average length of 1.6  $\mu\text{m}$  (Figure S5). X-ray diffraction patterns show the variation in abundance of FCC  $\text{Co}_9\text{S}_8$  to FCC  $\text{Co}^0$  as the  $\text{Co}^{\text{II}}:\text{Cys}$  mole ratio is varied from 0.9 to 9.7 (Figure 2g). TEM and SAED characterization of isolated  $\text{Co}_9\text{S}_8$  and Co nanowires from starting 0.9 and 4.9 ( $\text{Co}^{\text{II}}:\text{Cys}$ ) mole ratio solutions (respectively) is shown in Figure 3. The nanowires are high quality, single-crystal structures with smooth surfaces and negligible presence of structural defects such as stacking

faults. TEM characterization of a 60 nm  $\text{Co}_9\text{S}_8$  nanowire and the corresponding FFT is shown in Figure 3a. The nanowire is shown to have a well-defined, smooth edge with the presence of a 3 - 4 nm capping layer surrounding the nanowire. The selected area electron diffraction (SAED) pattern of the same

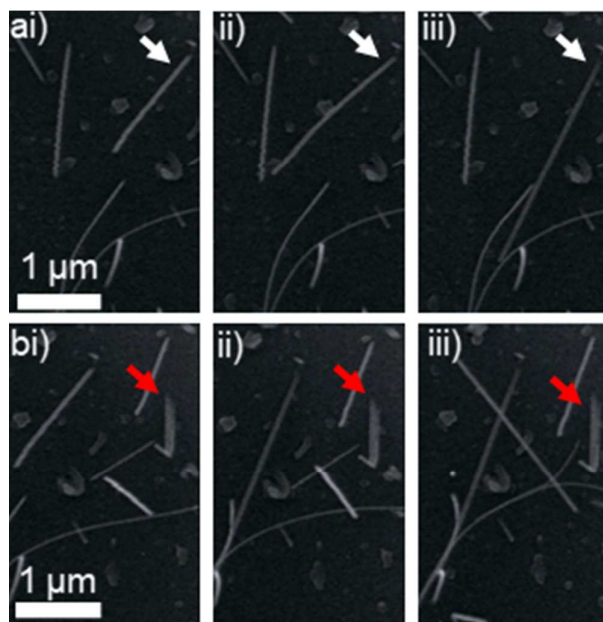


**Figure 4** Time-dependent SEM characterisation during  $\text{Co}_9\text{S}_8$  nanowire growth. **ai-iii)** SEM images showing a nanowire growth sequence over 95 seconds. **bi-iii)** Image sequence captured over a 10 minute period.

nanowire is shown in Figure 3b. Characterization by SAED shows the nanowire to be single-crystal. The SAED pattern was indexed as the FCC  $\text{Fm}\bar{3}\text{m}$  space group using the  $\text{Co}_9\text{S}_8$  parameters. The zone axis is [001] (Figure 3b). The {200} plane spacing was measured to be 4.8  $\text{\AA}$  in agreement with  $\text{Co}_9\text{S}_8$  ( $d_{\{200\}} = 4.964 \text{\AA}$ ). The nanowire growth direction was determined to be in the  $\langle 100 \rangle$  direction by the FFT and the shape factor induced streaking of the SAED pattern.<sup>58</sup> Figure 3c shows a TEM image of a cobalt nanowire with a 80 nm diameter and a capping layer. The SAED pattern (Figure 3d) was resolved along the [001] zone axis and the {200} plane spacing was measured to be 1.72  $\text{\AA}$  in agreement with FCC Co (1.772  $\text{\AA}$ ). The nanowire growth direction was  $\langle 110 \rangle$ . The growth direction was determined by the shape factor induced streaking of the diffraction intensity spots and correlated by the shadow imaging technique (Figure S6). Compositional analysis using energy dispersive X-ray spectroscopy (EDS) of isolated  $\text{Co}_9\text{S}_8$  and Co nanowires from 0.9 and 4.9 ( $\text{Co}^{\text{II}}:\text{Cys}$ ) precursor solutions (Figure S7) further supports XRD and SAED phase assignment.

Time-dependent FESEM characterization during nanowire growth is shown in Figure 4. Growth was achieved using a 0.9 ( $\text{Co}:\text{Cys}$ ) precursor solution and the substrate preparation procedure outlined in the experimental section. FESEM characterization was performed at a stabilized temperature (540  $^\circ\text{C}$ ) under high vacuum ( $9 \times 10^{-6}$  mbar). Images were captured at a constant magnification. The growth sequence of

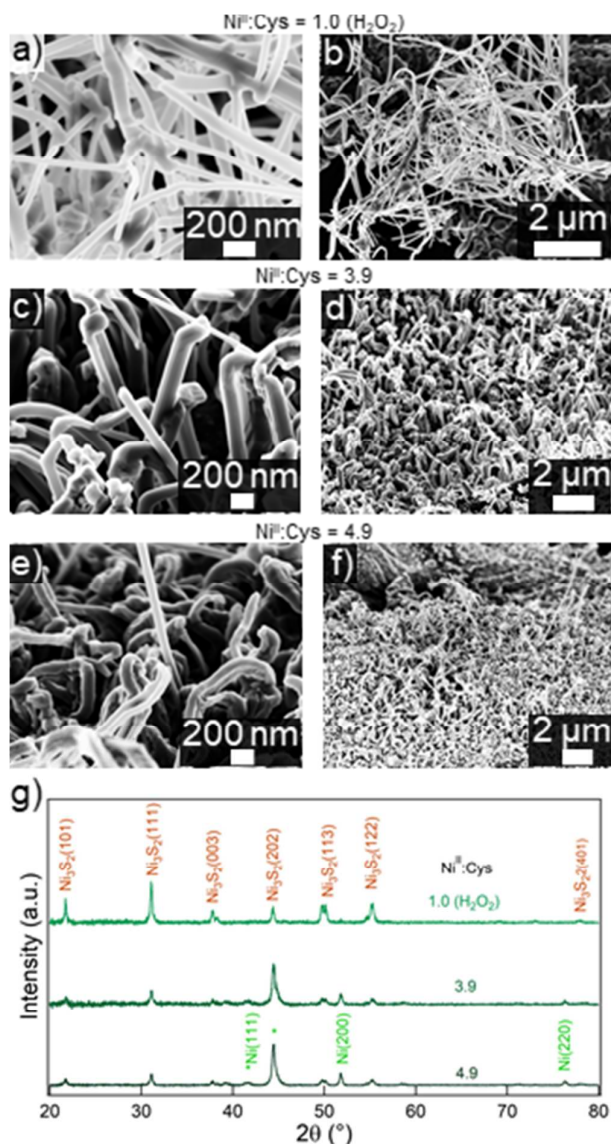


**Figure 5** SEM images of Ni<sub>3</sub>S<sub>2</sub> and Ni nanostructures grown from starting 1.0 (a and b), 3.9 (c and d) and 4.9 (e and f) Ni<sup>II</sup>:Cys mole ratio solutions. g) X-ray diffraction patterns of the nanostructures.

the two nanowires is shown in Figures 4ai-iii and Figures 4bi-iii respectively. Nanowires are shown to grow directly from the residual precursor film at the stabilized growth temperature. The results confirm nanowire growth at a stabilized temperature and not during cool down (or only during heat-up). Based on the characterization of the nanowire in Figures 4bi-iii) the unique shape of the tip supports the proposal that adatoms are incorporated into the nanowire below the film surface. Analogous to a base-driven growth mechanism. The method can also be used to synthesize Ni<sup>0</sup> and Ni<sub>3</sub>S<sub>2</sub> nanowires. Figures 5a and b show SEM images of nanowires grown by thermolysis of a 1.0 (Ni<sup>II</sup>:Cys) mole ratio solution, and the corresponding X-ray diffraction pattern is shown in Figure 5g. Nanowires of the rhombohedral phase Ni<sub>3</sub>S<sub>2</sub> (PDF 04-008-8458, Figure 5a and b) were obtained only after oxidation of

the precursor solution using 30% w/w H<sub>2</sub>O<sub>2</sub>. The resultant nanowires and nanorods had an average diameter of 66 nm based on an analysis of 59 structures (Figure S8).

Nanostructures grown from the 3.9 solution are shown in Figure 5c and d, where the resultant nanowires have an average diameter of 100 nm based on an analysis of 32 structures (Figure S9). The nanostructures had a mixture of phases, with the dominant phase being FCC Ni<sup>0</sup> (PDF 04-010-6148) and a minor presence of Ni<sub>3</sub>S<sub>2</sub> (Figure 3g). Thermolysis of the 4.9 solution resulted in nanostructures of the lowest aspect ratio (Figure 5e and f) composed of FCC Ni<sup>0</sup> with a minor presence of Ni<sub>3</sub>S<sub>2</sub> (Figure 5g). The presence of Ni<sub>3</sub>S<sub>2</sub> is

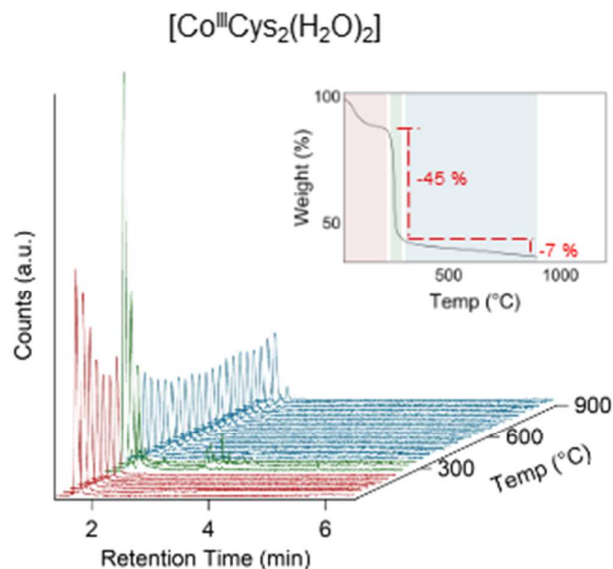


**Figure 6** Total ion chromatographs taken every 30 °C between 30 – 900 °C, the heating rate was 3 °C/min for cobalt(III) bis-cysteinate. (inset) Thermogravimetric data for cobalt(III) bis-cysteinate.

attributed to atmospheric oxidation of the dropcast and dried precursor solution.

Further characterization of individual Ni<sub>3</sub>S<sub>2</sub> and Ni nanowires was performed by energy dispersive X-ray spectroscopy (EDS), transmission electron microscopy (TEM) and selected area electron diffraction (SAED). The results confirm that the nanowires are single crystals, with the phases matching those determined by XRD (Figure S10). No nanowire growth was observed upon decomposition of only metal(II) acetate, in agreement with prior reports.<sup>59-63</sup>

**Precursor Chemistry.** Addition of cysteine to cobalt(II) salts forms a cobalt(III) bis-cysteinate complex.<sup>64</sup> Characterization of the isolated cobalt-cysteine complex by UV-vis absorbance (Figure S11a) and FTIR (Figure S13) confirms the octahedral coordination geometry with cysteine acting as a bidentate ligand via S and N donors to the cobalt(III) centre (see Supporting Information for further discussion).<sup>64-66</sup> High-resolution mass spectrometry of the isolated cobalt complex shows an isotope distribution pattern with a maximum intensity at  $m/z = 298.9580$ . Modelling of this distribution produces an excellent fit for a molecular formula of

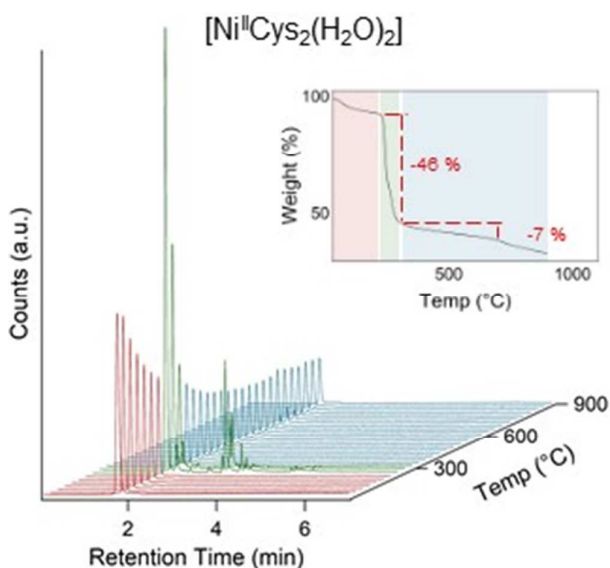


**Figure 7** Total ion chromatographs taken every 30 °C between 30 – 900 °C, the heating rate was 3 °C/min for nickel(II) bis-cysteinate. (inset) Thermogravimetric data for nickel(III) bis-cysteinate.

$[\text{CoC}_6\text{H}_{12}\text{N}_2\text{O}_4\text{S}_2]^+$ , with a mass deviation of 5ppm, confirming that the solution-state inner coordination sphere of the nanowire precursor contains one cobalt(III) and two cysteine units (cobalt(III) bis-cysteinate). The oxidation of cobalt(II) (in cobalt acetate) to cobalt(III) in the complex is attributed to exposure of the solution to atmospheric oxygen; the associated colour change can be slowed by degassing using  $\text{N}_2$  (Figure S14).<sup>67-69</sup> The UV-vis absorbance spectra of the 0.9 and 4.9 (Co<sup>II</sup>:Cys) precursor solutions (Figure S12a) show identical absorbance bands to the isolated complex (Figure S11a); the multiple band at 515 nm due to the cobalt(II) acetate is not observed as it is of low intensity ( $\epsilon = 4.6 \text{ M}^{-1}\text{cm}^{-1}$ ) and obscured by the precursor complex. The identical absorbance maximum in each of the precursor solutions indicates that the inner coordination sphere of the cobalt complex remains unchanged with varying Co<sup>II</sup>:Cys ratios.

UV-vis absorbance spectra for the 1.0, 3.9 and 4.9 nickel(II)-cysteine precursor solutions (Figure S12b) confirm the square planar  $d^8$  nickel(II) complexes in all solutions, and are in agreement with the solid state structure of  $\text{Ni}^{\text{II}}\text{Cys}_2$ .<sup>70</sup> The nickel(II) acetate bands expected at 395 ( $\epsilon = 5.0 \text{ M}^{-1}\text{cm}^{-1}$ ), and 724 nm ( $\epsilon = 2.0 \text{ M}^{-1}\text{cm}^{-1}$ ) due to  $\text{Ni}(\text{H}_2\text{O})_6^{2+}$  were not observed in the nanowire precursor solutions due to their low intensity. The precursor product in the 1.0 (Ni<sup>II</sup>:Cys) mole ratio solution could not be unambiguously identified following the addition of  $\text{H}_2\text{O}_2$ . The FTIR spectrum of the isolated nickel-cysteine product (Figure S13) shows bands similar to those of the  $[\text{Co}^{\text{III}}\text{Cys}_2(\text{H}_2\text{O})_2]$  spectrum (see Supporting Information for further discussion).

**Precursor Decomposition.** TGA-GC-MS of the isolated cobalt(III) bis-cysteinate ( $[\text{Co}^{\text{III}}\text{Cys}_2(\text{H}_2\text{O})_2]$ ) complex (Figure 6), shows that the coordinated cysteine is thermally stable to 180 °C before the onset of ligand decomposition, which occurs in a

three-step process. The first process occurs between 30 to 180 °C ( $\text{DTG}_{\text{max}} = 68 \text{ °C}$ ), with a mass loss of 10.2% attributed to the loss of coordinated water (Calc: 8.4%) and some residual moisture to produce anhydrous cobalt(III) bis-cysteinate. The temperature resolved extracted ion chromatographs for  $m/z = 18$  (Figure S15a) are in excellent agreement with the thermogravimetry, showing water present only between 30 and 180 °C with local maxima at 60 and 90 °C attributed to unbound water and coordinated water, respectively.

The next process occurs between 180 to 240 °C ( $\text{DTG}_{\text{max}} = 233 \text{ °C}$ ), with a mass loss of 5.3% attributed to the loss of carbon dioxide from the acetate anion (Calc: 10.3%). The mass discrepancy is due to an overlap between two thermal events;

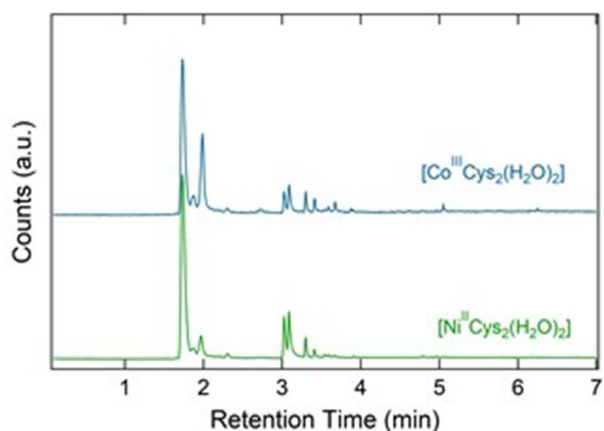


**Figure 8** Gas chromatograms of the thermolysis products at 270 °C for cobalt(III) bis-cysteinate (top) and nickel(II) bis-cysteinate (bottom).

the loss of  $\text{CO}_2$  from acetate and the loss of cysteine ligand moieties. The temperature resolved extracted ion chromatographs for  $m/z = 44$  (Figure S15c) are in excellent agreement with the thermogravimetry, showing carbon dioxide being present only between 180 and 240 °C with maximum abundance at 240 °C, correlating to the  $\text{DTG}_{\text{max}}$  of the acetate decomposition. The TGA suggests that after acetate decomposition, the charged  $[\text{Co}(\text{Cys})_2]^+$  species is produced as an intermediate, which spontaneously dissociates in the 240 to 300 °C range with a mass loss of 39.6% ( $\text{DTG}_{\text{max}} = 256 \text{ °C}$ ) to yield an unknown mixture of  $\text{Co}_x\text{S}_y$  sulfides. There is no further loss of volatile species attributed to decomposition of the Co(cys) complex beyond 300 °C (Figure 6 and Figure S15).

The final process involves the steady loss of sulfur between 300 to 900 °C from the intermediate  $\text{Co}_x\text{S}_y$  residue remaining after 300 °C, to yield a final product of  $\text{Co}_9\text{S}_8$  as determined by powder XRD of the TGA residue (Figure S16). The loss of sulfur is observed as sulfur dioxide due to gas phase reactions between sulfur and residual oxygen, and is the only volatile species produced beyond 300 °C (Figure 6 and Figure S15e).

TGA-GC-MS of nickel(II) bis-cysteinate (Figure 7) reveals similar thermal behaviour to that of cobalt(III) bis-cysteinate. The complex is thermally stable to 180 °C before the onset of ligand decomposition which occurs in a two-step process. In contrast to the decomposition of cobalt(III) bis-cysteinate,

there is no other mass loss due to carbon dioxide, which is attributed to the lack of acetate anions within the neutral nickel(II) bis-cysteinate ( $[\text{Ni}^{\text{II}}\text{Cys}_2(\text{H}_2\text{O})_2]$ ) complex. Between 220 and 290 °C the approximate 45% mass loss event is attributed to decarboxylation of the cysteine ligands followed by N- and S-containing heterocyclic species to form intermediate  $\text{Ni}_x\text{S}_y$  residue. Finally, there is a loss of sulfur above 300 °C (Figure S15f) to yield a final product of non-stoichiometric  $\text{Ni}_3\text{S}_{1.8}$  (as determined using XRD, Figure S17).

Total ion chromatographs of the volatile species for both  $[\text{Co}^{\text{III}}\text{Cys}_2(\text{H}_2\text{O})_2]$  and  $[\text{Ni}^{\text{II}}\text{Cys}_2(\text{H}_2\text{O})_2]$  shortly following the main decomposition step show a mixture of S- and N-heterocyclic species, water and carbon dioxide (Figure 8). Of these species, thiophene ( $R_t = 2:301$  min), 2-methyl-thiazole ( $R_t = 3:020$  min), 2-methyl-pyridine ( $R_t = 3:092$  min), 3-acetamido-pyrrolidine ( $R_t = 3:292$  min) and 2-methyl-2-thiazole were unambiguously assigned. The presence of these species is in agreement with the literature for thermal decomposition of cysteine at temperatures above 200 °C.<sup>71</sup> The absence of ammonia, and presence of heterocyclic nitrogenous compounds in the chromatographs strongly suggests that there was no cleavage of the C-N bond within the cysteine moieties. The presence of these heterocyclic species can be explained by intra-molecular cyclization of intermediate immonium ions formed by cleavage of the  $\text{CH} - \text{C} = \text{O}$  bond within the cysteine ligand.<sup>72, 73</sup> Similarly, the presence of  $\text{CO}_2$  and water is attributed to the decarboxylation of the amide moiety in the cysteine ligands. It can be inferred that a very similar thermal decomposition process is occurring during the thermolysis of these two precursors, given the similarity of the volatile species produced.

## Conclusions

The versatility of cysteine-based precursors is demonstrated in phase-controlled nanowire synthesis by solventless thermolysis.  $\text{Co}_9\text{S}_8$  and Co nanowires were realized by heat-up synthesis using the precursors cobalt(III) bis-cysteinate and cobalt(II) acetate, the phase was determined by the mole ratio. A similar strategy was successful in the  $\text{Ni}_3\text{S}_2/\text{Ni}$  system. Characterization of the nanowire phase, morphology, growth direction and composition is provided showing the nanowires to be high-quality structures with the presence of a capping layer. Understanding of the conversion reactions from precursor to nanowire is elucidated through detailed characterization of the precursors and reaction steps during thermolysis. Real-time characterization using FESEM confirms nanowire formation does in fact occur at the stabilized growth temperature (and not during cool down) and provides evidence for a base driven mechanism. The results are used to support analysis by TGA-GC-MS of the bis-cysteinate precursors. Analysis by TGA-GC-MS shows the cysteine ligands are thermally stable to 220 °C before undergoing decomposition. At temperatures greater than 300 °C the steady generation of  $\text{SO}_2$  is the only volatilized species observed. The generation of such species has been shown previously to support anisotropic growth in nanocrystals. The

results provide new insights into the reaction steps and moieties that support symmetry breaking growth in metal and metal sulfide nanocrystals.

## Conflicts of interest

There are no conflicts to declare.

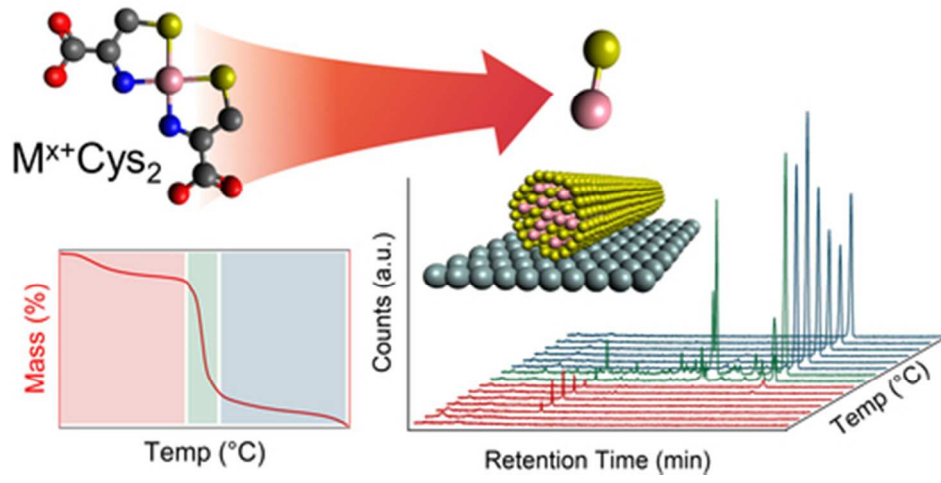
## Acknowledgements

This work was funded by the Australia Government through the Australian Research Council (DP140102721, DE130100592). The authors thank Dr. Marco Fronzi for useful discussions.

## References

- 1 A. Henglein, *J. Phys. Chem.*, 1982, **86**, 2291-2293.
- 2 C. B. Murray, C. Kagan and M. Bawendi, *Annu. Rev. Mater. Sci.*, 2000, **30**, 545-610.
- 3 J. Park, J. Joo, S. G. Kwon, Y. Jang and T. Hyeon, *Angew. Chem. Int. Ed.*, 2007, **46**, 4630-4660.
- 4 C. B. Murray, D. J. Norris and M. G. Bawendi, *J. Am. Chem. Soc.*, 1993, **115**, 8706-8715.
- 5 R. Rossetti and L. Brus, *J. Phys. Chem.*, 1982, **86**, 4470-4472.
- 6 Y. W. Jun, M. F. Casula, J. H. Sim, S. Y. Kim, J. Cheon and A. P. Alivisatos, *J. Am. Chem. Soc.*, 2003, **125**, 15981-15985.
- 7 Y. Zhai and M. Shim, *Chem. Mater.*, 2017, **29**, 2390-2397.
- 8 M. P. Hendricks, M. P. Campos, G. T. Cleveland, I. Jen-La Plante and J. S. Owen, *Science*, 2015, **348**, 1226-1230.
- 9 T. P. A. Ruberu, H. R. Albright, B. Callis, B. Ward, J. Cisneros, H.-J. Fan and J. Vela, *ACS Nano*, 2012, **6**, 5348-5359.
- 10 J. M. Rhodes, C. A. Jones, L. B. Thal and J. E. Macdonald, *Chem. Mater.*, 2017, **29**, 8521-8530.
- 11 N. T. Thanh, N. Maclean and S. Mahiddine, *Chem. Rev.*, 2014, **114**, 7610-7630.
- 12 Y. Guo, S. R. Alvarado, J. D. Barclay and J. Vela, *ACS Nano*, 2013, **7**, 3616-3626.
- 13 N. J. Freymeyer, P. D. Cunningham, E. C. Jones, B. J. Golden, A. M. Wiltrout and K. E. Plass, *Cryst. Growth Des.*, 2013, **13**, 4059-4065.
- 14 R. H. Kore, J. S. Kulkarni and S. K. Haram, *Chem. Mater.*, 2001, **13**, 1789-1793.
- 15 Y. Jiang, Y. Huang, H. Cheng, Q. Liu, Z. Xie, T. Yao, Z. Jiang, Y. Huang, Q. Bian and G. Pan, *J. Phys. Chem. C*, 2013, **118**, 714-719.
- 16 S. A. Empedocles, R. Neuhauser, K. Shimizu and M. G. Bawendi, *Adv. Mater.*, 1999, **11**, 1243-1256.
- 17 L. Qu, W. W. Yu and X. Peng, *Nano Lett.*, 2004, **4**, 465-469.
- 18 M. Liu, K. Wang, L. Wang, S. Han, H. Fan, N. Rowell, J. A. Ripmeester, R. Renoud, F. Bian and J. Zeng, *Nat. Commun.*, 2017, **8**, 15467.
- 19 J. S. Owen, E. M. Chan, H. T. Liu and A. P. Alivisatos, *J. Am. Chem. Soc.*, 2010, **132**, 18206-18213.
- 20 L. S. Hamachi, I. Jen-La Plante, A. C. Coryell, J. De Roo and J. S. Owen, *Chem. Mater.*, 2017, **29**, 8711-8719.
- 21 J. S. Steckel, B. K. Yen, D. C. Oertel and M. G. Bawendi, *J. Am. Chem. Soc.*, 2006, **128**, 13032-13033.
- 22 Y. K. Jung, J. I. Kim and J. K. Lee, *J. Am. Chem. Soc.*, 2010, **132**, 178-184.
- 23 K. Yu, X. Liu, T. Qi, H. Yang, D. M. Whitfield, Q. Y. Chen, E. J. Huisman and C. Hu, *Nat. Commun.*, 2016, **7**, 12223.

- 24 M. B. Sigman, A. Ghezelbash, T. Hanrath, A. E. Saunders, F. Lee and B. A. Korgel, *J. Am. Chem. Soc.*, 2003, **125**, 16050-16057.
- 25 T. H. Larsen, M. Sigman, A. Ghezelbash, R. C. Doty and B. A. Korgel, *J. Am. Chem. Soc.*, 2003, **125**, 5638-5639.
- 26 A. Ghezelbash, M. B. Sigman and B. A. Korgel, *Nano Lett.*, 2004, **4**, 537-542.
- 27 M. B. Sigman and B. A. Korgel, *Chem. Mater.*, 2005, **17**, 1655-1660.
- 28 A. Angeloski, A. R. Gentle, J. A. Scott, M. B. Cortie, J. M. Hook, M. T. Westerhausen, M. Bhadbhade, A. T. Baker and A. M. McDonagh, *Inorg. Chem.*, 2018, **57**, 2132-2140.
- 29 S.-H. Chang, M.-D. Lu, Y.-L. Tung and H.-Y. Tuan, *ACS Nano*, 2013, **7**, 9443-9451.
- 30 G. Du, W. Li and Y. Liu, *J. Phys. Chem. C*, 2008, **112**, 1890-1895.
- 31 Y. Zhou, Y. Zhu, G. Du and B. Xu, *J. Nanosci. Nanotechnol.*, 2013, **13**, 6934-6939.
- 32 J. Xu, Q. Wang, X. Wang, Q. Xiang, B. Liang, D. Chen and G. Shen, *ACS Nano*, 2013, **7**, 5453-5462.
- 33 H.-W. Chen, C.-W. Kung, C.-M. Tseng, T.-C. Wei, N. Sakai, S. Morita, M. Ikegami, T. Miyasaka and K.-C. Ho, *J. Mater. Chem. A*, 2013, **1**, 13759-13768.
- 34 Y. Yin, C. K. Erdonmez, A. Cabot, S. Hughes and A. P. Alivisatos, *Adv. Funct. Mater.*, 2006, **16**, 1389-1399.
- 35 C.-C. Lin, S. J. Tan and J. Vela, *J. Mater. Chem. A*, 2017, **5**, 20351-20358.
- 36 N. D. Loh, S. Sen, M. Bosman, S. F. Tan, J. Zhong, C. A. Nijhuis, P. Král, P. Matsudaira and U. Mirsaidov, *Nat. Chem.*, 2017, **9**, 77.
- 37 X. Huang, Z. J. Wang, G. Weinberg, X. M. Meng and M. G. Willinger, *Adv. Funct. Mater.*, 2015, **25**, 5979-5987.
- 38 B. Kim, J. Tersoff, S. Kodambaka, M. Reuter, E. Stach and F. Ross, *Science*, 2008, **322**, 1070-1073.
- 39 C.-Y. Wen, M. Reuter, J. Bruley, J. Tersoff, S. Kodambaka, E. Stach and F. Ross, *Science*, 2009, **326**, 1247-1250.
- 40 J. Hannon, S. Kodambaka, F. Ross and R. Tromp, *Nature*, 2006, **440**, 69.
- 41 J. A. Scott, D. Totonjian, A. A. Martin, T. T. Tran, J. Fang, M. Toth, A. M. McDonagh, I. Aharonovich and C. J. Lobo, *Nanoscale*, 2016, **8**, 2804-2810.
- 42 K.-Y. Jiang, Y.-L. Weng, S.-Y. Guo, Y. Yu and F.-X. Xiao, *Nanoscale*, 2017, **9**, 16922-16936.
- 43 F. Teng, L. Zheng, K. Hu, H. Chen, Y. Li, Z. Zhang and X. Fang, *J. Mater. Chem. C*, 2016, **4**, 8416-8421.
- 44 J. Xu, W. Yang, H. Chen, L. Zheng, M. Hu, Y. Li and X. Fang, *J. Mater. Chem. C*, 2018, **6**, 3334-3340.
- 45 H. Lee, Y. Yoo, T. Kang, J. Lee, E. Kim, X. Fang, S. Lee and B. Kim, *Nanoscale*, 2016, **8**, 10291-10297.
- 46 H. Wei, D. Pan, S. Zhang, Z. Li, Q. Li, N. Liu, W. Wang and H. Xu, *Chem. Rev.*, 2018, **118**, 2882-2926.
- 47 L. Mai, X. Tian, X. Xu, L. Chang and L. Xu, *Chem Rev*, 2014, **114**, 11828-11862.
- 48 Z.-x. Yang, N. Han, M. Fang, H. Lin, H.-Y. Cheung, S. Yip, E.-J. Wang, T. Hung, C.-Y. Wong and J. C. Ho, *Nat. Commun.*, 2014, **5**, 5249.
- 49 D. Xu, Z. Liu, J. Liang and Y. Qian, *J. Phys. Chem. B*, 2005, **109**, 14344-14349.
- 50 P. Reiss, M. Carrière, C. Lincheneau, L. Vaure and S. Tamang, *Chem. Rev.*, 2016, **116**, 10731-10819.
- 51 M. Afzaal, M. A. Malik and P. O'Brien, *J. Mater. Chem.*, 2010, **20**, 4031-4040.
- 52 H. Liu, J. S. Owen and A. P. Alivisatos, *J. Am. Chem. Soc.*, 2007, **129**, 305-312.
- 53 R. Himstedt, P. Rusch, D. Hinrichs, T. Kodanek, J. Lauth, S. Kinge, L. D. A. Siebbeles and D. Dorfs, *Chem. Mater.*, 2017, **29**, 7371-7377.
- 54 Z. Chen, R. Wu, M. Liu, H. Wang, H. Xu, Y. Guo, Y. Song, F. Fang, X. Yu and D. Sun, *Adv. Funct. Mater.*, 2017, **27**.
- 55 W. He, C. Wang, H. Li, X. Deng, X. Xu and T. Zhai, *Adv. Energy Mater.*, 2017, **7**, 1700983.
- 56 Y. Hou, M. Qiu, G. Nam, M.-G. Kim, T. Zhang, K. Liu, X. Zhuang, J. Cho, C. Yuan and X. Feng, *Nano Lett.*, 2017, **17**, 4202-4209.
- 57 P. Chen, T. Zhou, M. Zhang, Y. Tong, C. Zhong, N. Zhang, L. Zhang, C. Wu and Y. Xie, *Adv. Mater.*, 2017, **29**, 1701584.
- 58 Y. Ding and Z. L. Wang, *J. Phys. Chem. B*, 2004, **108**, 12280-12291.
- 59 T. Wanjun and C. Donghua, *Chem. Pap.*, 2007, **61**, 329-332.
- 60 M. Mohamed, S. Halawy and M. Ebrahim, *J. Therm. Anal. Calorim.*, 1994, **41**, 387-404.
- 61 E. Ingier-Stocka and A. Grabowska, *J. Therm. Anal. Calorim.*, 1998, **54**, 115-123.
- 62 R. W. Grimes and A. N. Fitch, *J. Mater. Chem.*, 1991, **1**, 461-468.
- 63 J. C. De Jesus, I. González, A. Quevedo and T. Puerta, *J. Mol. Catal. A: Chem.*, 2005, **228**, 283-291.
- 64 R. G. Neville and G. Gorin, *J. Am. Chem. Soc.*, 1956, **78**, 4893-4896.
- 65 A. B. P. Lever, *Inorganic Electronic Spectroscopy*, Elsevier, Amsterdam, Netherlands, 1968.
- 66 S. F. Parker, *Chem. Phys.*, 2013, **424**, 75-79.
- 67 M. P. Schubert, *J. Am. Chem. Soc.*, 1931, **53**, 3851-3861.
- 68 R. G. Neville and G. Gorin, *J. Am. Chem. Soc.*, 1956, **78**, 4891-4893.
- 69 C. Bresson, R. Spezia, S. Esnouf, P. L. Solari, S. Coantic and C. Den Auwer, *New J. Chem.*, 2007, **31**, 1789-1797.
- 70 N. Baidya, D. Ndreu, M. M. Olmstead and P. K. Mascharak, *Inorg. Chem.*, 1991, **30**, 2448-2451.
- 71 V. Yablokov, Y. A. Vasina, I. Zelyaev and S. Mitrofanova, *Russ. J. Gen. Chem.*, 2009, **79**, 1141-1145.
- 72 A. K. Lam, V. Ryzhov and A. Richard, *J. Am. Soc. Mass. Spectrom.*, 2010, **21**, 1296-1312.
- 73 V. Ryzhov, A. K. Lam and A. Richard, *J. Am. Soc. Mass. Spectrom.*, 2009, **20**, 985-995.



39x19mm (300 x 300 DPI)